Supplement of Atmos. Chem. Phys., 24, 11679–11699, 2024
https://doi.org/10.5194/acp-24-11679-2024-supplement

Supplement of

Ether and ester formation from peroxy radical recombination: a qualitative reaction channel analysis

Lauri Franzon et al.

Correspondence to: Lauri Franzon (lauri.franzon@helsinki.fi) and Theo Kurtén (theo.kurten@helsinki.fi)

Contents

S1 Parametrization of the Effective Hydrogen Bond Number **S2**

S2 Correcting Recombination Yields for $RC(O)O_2$ H-shift Rates **S5**

S3 Computations on α-NO_2 ejection reaction **S8**

S4 Accuracy of Nannoolal Vapour Pressures **S11**

S5 Sensitivity Analysis of the Yield filter **S12**

S6 Vapour Pressure Visualisations **S14**
S6.1 DTA Dataset S14
S6.2 Terpene Dataset S15
S6.3 β-caryophyllene Dataset S16

S7 Tables on distributions of accretion product properties **S17**
S7.1 Distribution by Reaction Channel S17
S7.2 Distribution by Precursor Molecule S18
S7.3 Distribution by VOC Oxidant S20
S7.4 Distribution by RO_2 class S21

S8 Technical Details on Estimation of Atmospheric Concentrations **S22**

S1 Parametrization of the Effective Hydrogen Bond Number

When looking for an ideal HBN parametrization to filter out weakly bounded ^{3}(RO...OR) complexes, we must first determine a limit for weak binding. As we have established that the ISC rate forming the ROOR product is often of order $k_{ISC} \approx 10^9$ s^{-1}, a suitable choice would be to pick the binding energy corresponding the the dissociation rate $k_d \approx 10^8$ s^{-1}. The relationship between the energies and the dissociation rates calculated in our previous work (Franzon, 2023) is presented in Figure S1.

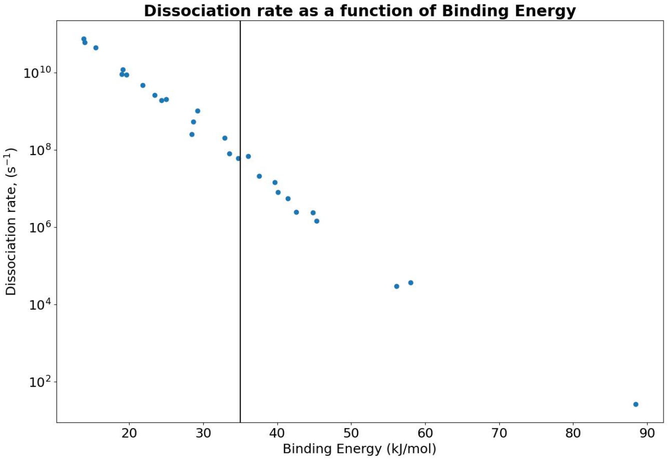

Figure S1. Dissociation rates calculated in Franzon (2023) as a function of complex binding energy. A vertical line is drawn at 35 kJ/mol to demonstrate that this is where the $10k_d < k_{ISC} = 10^9$ s^{-1}.

As we have noted previously, C-H bonds have shown weak H-bond donor behaviour in computational studies on ^{3}(RO...OR) complexes. The 'partial H-bond donor value' ascribed to these bonds was determined by calculating the HBN values for all 31 ^{3}(RO...OR) from Hasan (2023) using various values for the CH bond and searching for the best correlation between the binding energy and the HBN. The results are presented in Figure S2 and in Table S1. As seen in the figure, the partial donor value of 0.04 gave the best correlation, and this was thus used in the code.

$$HBN_{\alpha,\beta} = n_{\mathrm{D},\alpha} \cdot n_{\mathrm{A},\beta} + n_{\mathrm{D},\beta} \cdot n_{\mathrm{A},\alpha} \quad (1)$$

Of course, this approach of estimating the binding energy using only the H-bonding properties ignores the impact of molecular geometry, as exemplified by the $^3(\mathrm{RO}\ldots\mathrm{OR})$ complexes with optical isomers. For these systems, the average over all isomers was used in the fit. In theory, this introduces errors due to not treating these isomers identically in the code. However, molecules with such geometric constraints are likely to be larger, with more than enough H-bonding groups to make it over the threshold of inclusion. If this assumption is correct, the deficiencies of this H-bonding model will not matter, as we are only using it to rule out too weakly bonded complexes. In the linear fit presented in Figure S3, the HBN value corresponding to the binding energy 35 kJ/mol was 1.76. We rounded this value down to 1.75 to use as a cutoff in the code. As seen in Figure S3, this leaves out a few complexes with binding energies slightly above 35 kJ/mol, namely ProO-ProOHO, EtO-BuOHO and EtO-ProOHO (See Table S1). However, these complexes all have dissociation rates at the lower end of the competitive range ($k_d > 10^7$ s^{-1}) and intermolecular H-shift rates above 10^8 s^{-1} (Hasan et al., 2023). The somewhat stricter HBN cutoff may be seen as an acceptable compromise to more certainly rule out the vast majority of complexes where reaction channels R1 and R2 are dominant.

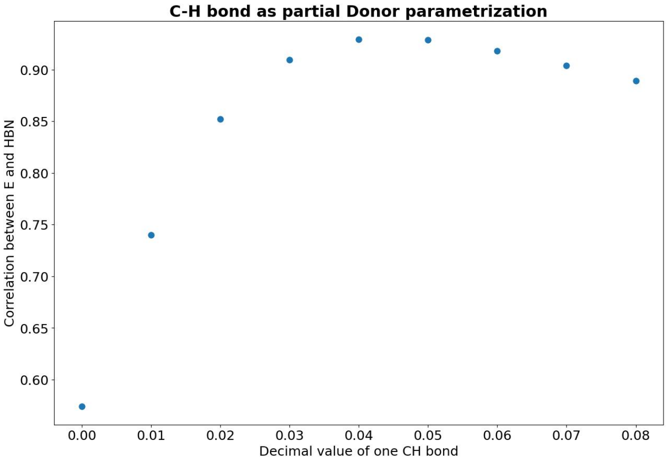

Figure S2. Correlation between effective H-Bond number and binding energies with various fractional donor values assigned to the C-H bonds.

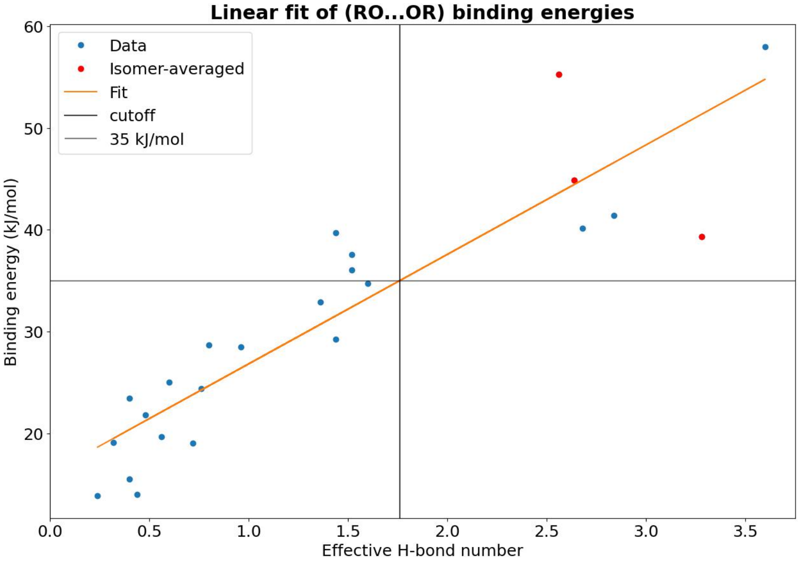

Figure S3. Linear fits of the $^3(\mathrm{RO}\ldots\mathrm{OR})$ binding energy as a function of the effective H-bond number, with optical isomer effects averaged. The fit coefficient is $R^2 = 0.818$.

Complex	$\Delta E \frac{\text{kJ}}{\text{mol}}$	$\ln k_d$	$n_{\text{CH},\alpha}$	$n_{D,\alpha}$	$n_{A,\alpha}$	$n_{\text{CH},\beta}$	$n_{D,\beta}$	$n_{A,\beta}$	HBN
(MetO)$_2$	13.89	10.88	3	0	1	3	0	1	0.24
(EtO)$_2$	23.46	9.41	5	0	1	5	0	1	0.4
(ProO)$_2$	19.65	9.95	7	0	1	7	0	1	0.56
(AceO)$_2$	28.68	8.73	5	0	2	5	0	2	0.8
(ButO)$_2$	19.03	9.96	9	0	1	9	0	1	0.72
R,R-(BuOHO)$_2$	56.15	4.47	8	1	1	8	1	1	2.64
R,S-(BuOHO)$_2$	33.57	7.91	8	1	1	8	1	1	2.64
(PrNO$_3$)$_2$	28.48	8.40	6	0	2	6	0	2	0.96
R-alk,R-nitr-α-pin	44.81	6.38	16	0	2	16	0	2	2.56
R-alk,S-nitr-α-pin	42.59	6.39	16	0	2	16	0	2	2.56
S-alk,R-nitr-α-pin	88.45	1.43	16	0	2	16	0	2	2.56
S-alk,S-nitr-α-pin	45.31	6.16	16	0	2	16	0	2	2.56
S-alk,R-hydr-α-pin	38.24	-[a]	16	1	1	16	1	1	3.28
R-alk,S-hydr-α-pin	38.07	-[a]	16	1	1	16	1	1	3.28
S-alk,S-hydr-α-pin	40.84	-[a]	16	1	1	16	1	1	3.28
R-alk,R-hydr-α-pin	40.04	-[a]	16	1	1	16	1	1	3.28
(α-pin-O$_3$−RO)$_2$[b]	58	4.57	15	0	3	15	0	3	3.6
MetO-EtO	19.12	10.08	3	0	1	5	0	1	0.32
MetO-ProO	15.48	10.65	3	0	1	7	0	1	0.4
MetO-AceO	13.97	10.78	3	0	1	5	0	2	0.44
MetO-ProOHO	32.93	8.30	3	0	1	6	1	1	1.36
MetO-BuOHO	29.25	9.01	3	0	1	8	1	1	1.44
EtO-ProO	21.84	9.67	5	0	1	7	0	1	0.48
EtO-AceO	25.02	9.31	5	0	1	5	0	2	0.6
EtO-ProOHO	39.71	7.16	5	0	1	6	1	1	1.44
EtO-BuOHO	36.07	7.83	5	0	1	8	1	1	1.52
ProO-AceO	24.39	9.28	7	0	1	5	0	2	0.76
ProO-ProOHO	37.57	7.32	7	0	1	6	1	1	1.52
ProO-BuOHO	34.75	7.78	7	0	1	8	1	1	1.6
AceO-ProOHO	40.12	6.90	5	0	2	6	1	1	2.68
AceO-BuOHO	41.42	6.75	5	0	2	8	1	1	2.84

Table S1. Dissociation rates, binding energies, and HBN calculations for the ^{3}(RO . . . OR) complexes from (Hasan, 2023). [a] The dissociation rates were never calculated by Franzon (2023), but we can likely assume that they would be lower than 10^8 s^{-1} by extrapolation from observed trends. [b] From Peräkylä et al. (2023).

S2 Correcting Recombination Yields for $RC(O)O_2$ H-shift Rates

As described in Sect. 2.1.2 of the main text, pairs of RO_2 are filtered by their recombination yields y, which are determined from the relative values of $k_{\mathrm{RO_2RO_2}}$ rate coefficients. Below the scheme is described with which we have accounted for the competition between $RO_2 + RO_2$ reactions and other bimolecular reactions of RO_2.

We must also consider the fact that $RO_2 + RO_2$ yields are also impacted by the other reaction rates of the radicals. We will start from a simplified equation where unimolecular RO_2 reaction are neglected, and where the peroxy radicals form an uniform 'pool' with concentration $[RO_2]$. In this case the yield of $RO_2 + RO_2$ is:

$$y_{\mathrm{RO_2RO_2}} = \frac{k_{\mathrm{RO_2RO_2}}[\mathrm{RO_2}]^2}{k_{\mathrm{RO_2RO_2}}[\mathrm{RO_2}]^2 + \sum_i^5 k_i[\mathrm{Ox}]_\mathrm{i}[\mathrm{RO_2}]} \tag{2}$$

Where the summation is over the other five bimolecular reactions: $RO_2 + NO$, $RO_2 + NO_2$, $RO_2 + NO_3$, $RO_2 + OH$ and $RO_2 + HO_2$. [Ox] is the concentration for one of these five reactants. The $RO_2 + RO_2$ reaction being a minor RO_2 loss in most atmospheric conditions, it is notable that the relationship between $y_{\mathrm{RO_2RO_2}}$ and $[RO_2]$ is linear at low concentrations: $y_{\mathrm{RO_2RO_2}} \approx \frac{k_{\mathrm{RO_2RO_2}}}{\sum_i^5 k_i[\mathrm{Ox}]_i}[\mathrm{RO_2}]$. Next, we will derive the ratio of $y_{\mathrm{RO_2RO_2}}$ between two RO_2 with different rate coefficients but identical concentrations:

$$\begin{aligned}\frac{y_{\mathrm{RO_2RO_2},\alpha}}{y_{\mathrm{RO_2RO_2},\beta}} &= \frac{k_{\mathrm{RO_2RO_2},\alpha}}{k_{\mathrm{RO_2RO_2},\beta}} \times \frac{k_{\mathrm{RO_2RO_2},\beta}[\mathrm{RO_2}]^2 + \sum_i^5 k_{i,\beta}[\mathrm{Ox}]_i[\mathrm{RO_2}]}{k_{\mathrm{RO_2RO_2},\alpha}[\mathrm{RO_2}]^2 + \sum_i^5 k_{i,\alpha}[\mathrm{Ox}]_i[\mathrm{RO_2}]}\\ &\approx \frac{k_{\mathrm{RO_2RO_2},\alpha}}{k_{\mathrm{RO_2RO_2},\beta}} \times \frac{\sum_i^5 k_{i,\beta}[\mathrm{Ox}]_i}{\sum_i^5 k_{i,\alpha}[\mathrm{Ox}]_i}\end{aligned}$$

As we see, this ratio is a constant at the low $[RO_2]$ limit. Next, we need to consider whether the $\frac{\sum_i^5 k_{i,\beta}[\mathrm{Ox}]_i}{\sum_i^5 k_{i,\alpha}[\mathrm{Ox}]_i}$ may play a role in shifting specific recombination yields up or down. In their review and parametrization of RO_2 reaction rates and branching ratios, Jenkin et al. (2019) recommend using a single generic reaction rate for all $RO_2 + OH$ reactions. For the three $RO_2 + NO_x$ reactions, one generic rate is recommended for alkyl RO_2 and a second for acyl RO_2. The same is suggested for the $RO_2 + HO_2$ reaction, both with an additional RO_2 size-dependent factor $(1 - \mathrm{e}^{-0.23 n_{HA}})$, where n_{HA} is the number of non-H atoms in the R functionality. Differences caused by this factor are all within a factor of 2 for $n_{HA} > 3$ and within a factor of 1.1 for $n_{HA} > 10$, so likely this will only cause significant differences in lifetimes for small RO_2 in HO_2-dominated conditions. In summary, then, the relative impact of the $\frac{\sum_i^5 k_{i,\beta}[\mathrm{Ox}]_i}{\sum_i^5 k_{i,\alpha}[\mathrm{Ox}]_i}$ 'rate-to-yield'-factor on RO_2 recombination yields only needs to be considered for $RC(O)O_2$. In theory the value of this factor depends on the concentrations of the bimolecular reactants NO, NO_2, NO_3, OH and HO_2, as well as on the $RC(O)O_2$ size. However, for code optimization purposes we would prefer to use a single value that does not need to be calculated separately, and that neither overrepresents high-NO_x or low-NO_x conditions. For this reason, the following arbitrary intermediate level values were chosen for each reactant: $[\mathrm{NO}] = [\mathrm{NO_2}] = 2 \cdot 10^9$ molecule $\mathrm{cm^{-3}}$ (100 ppt), $[\mathrm{NO_3}] = 10^8$ molecule $\mathrm{cm^{-3}}$, $[\mathrm{OH}] = 10^6$ molecule $\mathrm{cm^{-3}}$, $[\mathrm{HO_2}] = 10^7$ molecule $\mathrm{cm^{-3}}$. With these concentrations the value of the rate-to-yield factor for $RC(O)O_2$ is 0.56.

Correcting the yields using the rates of competing *unimolecular* reactions is harder, as GECKO-A does not support RO_2 H-shift reactions (Often referred to as autoxidation, as this immediately results in O_2 addition to the product radical (Bianchi et al., 2019)) at the time of writing. These are known to be especially fast for $RC(O)O_2$ (Vereecken and Nozière, 2020; Seal et al., 2023), which incidentally also have rapid recombination rates with virtually all other RO_2's (Jenkin et al., 2019). Accounting for the effect of unimolecular decay on the $RC(O)O_2$ recombination yields is thus especially important, as these reactions will otherwise be over-represented in our data. The impact that the autoxidation rate has on the recombination yield for $RC(O)O_2$'s ($y_{\mathrm{RO_2RO_2},9}$) is modelled using Eq. 3 and compared to the recombination yields of the three next RO_2 classes for reference in

Figure S4. As seen in the figure, an autoxidation rate of $0.1\ \mathrm{s}^{-1}$ depresses $y_{\mathrm{RO_2RO_2},9}$ below $y_{\mathrm{RO_2RO_2},8}$, and a rate of $1\ \mathrm{s}^{-1}$ depresses it below $y_{\mathrm{RO_2RO_2},7}$, but even if if this is the case, $\mathrm{RO_2} + \mathrm{RC(O)O_2}$ reactions will still be among the more important $\mathrm{RO_2} + \mathrm{RO_2}$ reactions.

$$y_{\mathrm{RO_2RO_2}} = \frac{k_{\mathrm{RO_2RO_2}}[\mathrm{RO_2}]^2}{k_{\mathrm{RO_2RO_2}}[\mathrm{RO_2}]^2 + k_{auto}[\mathrm{RO_2}] + \sum_i^5 k_i[\mathrm{Ox}]_\mathrm{i}[\mathrm{RO_2}]} \qquad (3)$$

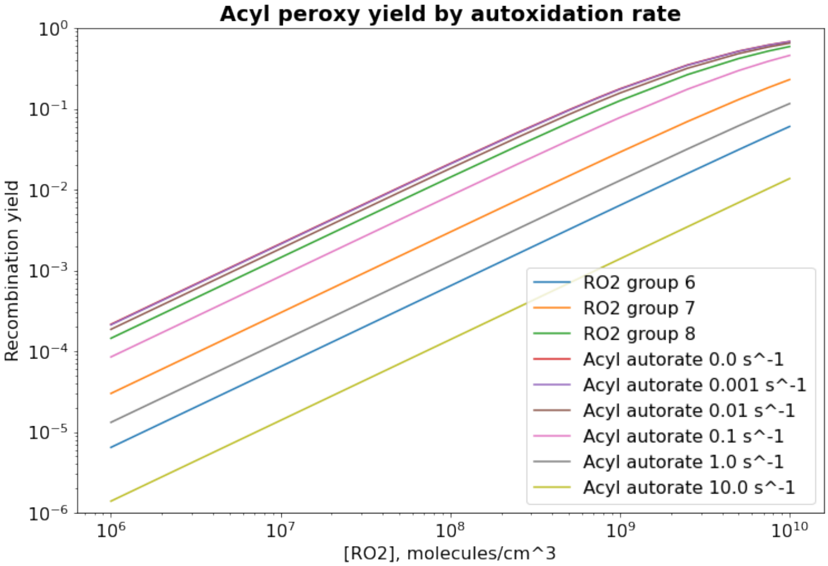

Figure S4. The impact that different $\mathrm{RC(O)O_2}$ autoxidation rates have on $y_{\mathrm{RO_2RO_2},9}$ relative to $y_{\mathrm{RO_2RO_2},8}$, $y_{\mathrm{RO_2RO_2},7}$ and $y_{\mathrm{RO_2RO_2},6}$. The yields are calculated assuming the representative intermediate concentrations $[\mathrm{NO}] = [\mathrm{NO_2}] = 2 \cdot 10^9$ molecule cm^{-3} (100 ppt), $[\mathrm{NO_3}] = 10^8$ molecule cm^{-3}, $[\mathrm{OH}] = 10^6$ molecule cm^{-3}, $[\mathrm{HO_2}] = 10^7$ molecule cm^{-3}.

Next, we need to evaluate how fast the $\mathrm{RC(O)O_2}$ autoxidation rates actually are relative to the bimolecular reactions. This information is presented in Table S2, adapted from Seal et al. (2023). According to this computational study, autoxidation rates of simple $\mathrm{RC(O)O_2}$ with four or more carbons are typically on the order of $0.1\ \mathrm{s}^{-1}$. Based on earlier computational results, (Rissanen et al., 2014) these autoxidation rates can also be as high as $3.8\ \mathrm{s}^{-1}$ or $7.5\ \mathrm{s}^{-1}$ for acidic H atoms at ideal spans. However, as GECKO-A currently lacks a general autoxidation rate calculator, the approach taken for this work was to assume an uniform $\mathrm{RC(O)O_2}$ autodixation rate of $1\ \mathrm{s}^{-1}$, which sits in the upper-limit range for generic $\mathrm{RC(O)O_2}$ autoxidation.

$RC(O)O_2$	Total	Approx
$MetC(O)O_2$	$7.3 \cdot 10^{-8}$	0
$EtC(O)O_2$	$9.0 \cdot 10^{-5}$	0
$PropC(O)O_2$	$1.0 \cdot 10^{-2}$	0.01
$ButC(O)O_2$	$6.9 \cdot 10^{-2}$	0.1
$PentC(O)O_2$	$2.0 \cdot 10^{-1}$	0.5
$HexC(O)O_2$	$4.2 \cdot 10^{-1}$	1
$SepC(O)O_2$	$2.5 \cdot 10^{-1}$	1
$OctC(O)O_2$	$4.5 \cdot 10^{-1}$	1

Table S2. The total autoxidation rate of simple acyl peroxy radicals as calculated by Seal et al. (2023). These rates are sums of the span-specific 1,n-H-shift rates presented in the original source.

An exception was made for the simplest and most common acyl peroxy radical, $CH_3C(O)O_2$, as this compound has a non-existent autoxidation rate (See Table S2) and a high ambient tropospheric concentration. (Villenave et al., 1998) Taken 90 together, these facts imply that $CH_3C(O)O_2$ is the most likely RO_2 recombination partner for many radicals with otherwise slow $RO_2 + RO_2$ rates, justifying a special treatment in the rate filtering code. The values used for the recombination rate and yield correction factor are presented in Table S3.

Pair	Rate ($\frac{\mathrm{cm}^3}{\mathrm{molecule\ s}}$)	f_α
$RC(O)O_2 + RO_2$	$1.1 \cdot 10^{-11}$	0.035
$RC(O)O_2 + RC(O)O_2$	$1.4 \cdot 10^{-11}$	0.035
$CH_3C(O)O_2 + RO_2$	$1.1 \cdot 10^{-11}$	0.56
$CH_3C(O)O_2 + CH_3C(O)O_2$	$1.6 \cdot 10^{-11a}$	0.56
$CH_3C(O)O_2 + RC(O)O_2$	$1.4 \cdot 10^{-11}$	0.035

Table S3. Autoxidation-corrected recombination yield values for $RC(O)O_2$ reactions and uncorrected values for $MetC(O)O_2$ reactions.
[a] IUPAC task group recommendation.

S3 Computations on α-NO_2 ejection reaction

As the occurrence or non-occurrence of the α-NO_2 ejection reaction in the $^3(\mathrm{RO}\ldots\mathrm{OR})$ complex proved to be of interest for accretion product inhibition (See Sect. 3.3 in the main text), the exact reaction rate of the reaction is a crucial detail. Thus the rate was computed for a set of four reference systems: $CH_2(NO_2)O\cdot$, $CH_3CH(NO_2)O\cdot$, $(CH_3)_2C(NO_2)O\cdot$, and $CH_2{=}CH(CH_3)C(NO_2)O\cdot$. The first of these is practically never important in the atmosphere, but as it is the simplest possible α-NO_2 RO its result can be treated as a good reference rate for the importance of substituent effects relative to $CH_3CH(NO_2)O\cdot$ and $(CH_3)_2C(NO_2)O\cdot$, which are the more relevant simple α-NO_2 systems. $CH_2{=}CHC(NO_2)O\cdot CH_3$ was included as a fourth model system as the α-C=C substituent is fairly common for these radicals (19 out of 49 α-NO_2 RO_2 in the DTA dataset) owing to the fact that these radicals are derived from aromatic oxidation. This substituent is also known to speed up RO β-scissions. (Vereecken and Peeters, 2009)

All calculations were performed using the ORCA 5.0.4 program. Neese (2022) The molecular geometries and transition state saddle points were calculated using the ωB97X-D3 density functional (Lin et al., 2013) and the jun-cc-pV(T+d)Z basis set (Papajak et al., 2011). Full conformer searches were performed for both the reactants and transition states using CREST, (Pracht et al., 2020) and the reaction rates were calculated using Multi-Conformer Transition State Theory: (Møller et al., 2016)

$$k_{MC-TST} = \frac{k_B T}{h} \frac{\sum_i^{n_{TS}} \kappa_i \mathrm{e}^{-\frac{G_i^{\ddagger}}{k_B T}}}{\sum_j^{n_R} \mathrm{e}^{-\frac{G_j}{k_B T}}} \tag{4}$$

where n_{TS} is the number of transition states found for the reaction, $G_i^{\ddagger}$ is the Gibbs free energy difference between the transition state and the global minimum reactant conformer, and κ_i is a tunneling coefficient calculated individually for each transition state. n_R is the number of reactant conformers and G_j is the Gibbs free energy difference of the reactant conformer relative to the global minimum, and k_B is the Boltzmann constant, h is the Planck constant, and T is the temperature. The equation is rearranged somewhat from the original source to better accommodate the fact that the ORCA output gives free energy and entropy values (with low frequencies corrected using the Grimme Quasi-Harmonic approximation, Grimme (2012)) but not thermodynamic partition functions. The tunneling coefficients κ_i were calculated using the Eckart approach (Eckart, 1930; Johnston and Heicklen, 1962), using the Zero-point corrected energies of the reactant, transition state and product, where the latter was received by performing an Intrinsic Reaction Coordinate (Ishida et al., 1977) at the B3LYP/def2-SVP level of theory (Stephens et al., 1994) and optimizing the resulting weakly bounded $RC{=}O + \cdot NO_2$ complex at the ωB97X-D3/jun-cc-pV(T+d)Z level. Conformer searches were not performed on the $C{=}O + NO_2$ product complex, as conformer differences in the reactant and TS were mainly caused by rotation of the breaking C-N bond. Thus, for the $CH_2{=}CHC{=}OCH_3 + NO_2$ system only the two conformers arising from the $\angle(\mathrm{C{=}O}, \mathrm{C{=}C})$ angle were considered, and for the other systems all TS were assumed to connect to the same product complex conformer. The results of the calculations are presented separately for each of the found transition states in Table S4.

	$E_i^\ddagger$ ($\frac{\text{kJ}}{\text{mol}}$)	$G_i^\ddagger$ ($\frac{\text{kJ}}{\text{mol}}$)	ω_i (cm^{-1})	κ_i	k_i (s^{-1})	k_{MC-TST} (s^{-1})	ΔH ($\frac{\text{kJ}}{\text{mol}}$)
$CH_2(NO_2)O\cdot$	27.16	26.90	-1067.74	3.39	$4.07 \cdot 10^8$	$4.07 \cdot 10^8$	-73.02
$CH_3CH(NO_2)O\cdot$ (TS 1)	21.99	21.58	-1048.09	3.06	$3.15 \cdot 10^9$		
$CH_3CH(NO_2)O\cdot$ (TS 2)	23.88	23.43	-1254.55	5.01	$2.45 \cdot 10^9$	$2.97 \cdot 10^9$	-94.26
$(CH_3)_2C(NO_2)O\cdot$ (TS 1)	20.01	20.12	-1264.69	4.63	$8.58 \cdot 10^9$		
$(CH_3)_2C(NO_2)O\cdot$ (TS 2)	15.95	20.55	-1264.24	4.07	$6.35 \cdot 10^9$	$1.41 \cdot 10^{10}$	-108.82
$CH_2{=}CHC(NO_2)O\cdot CH_3$ (TS 1)	15.14	15.14	-1128.60	3.12	$4.32 \cdot 10^{10}$		
$CH_2{=}CHC(NO_2)O\cdot CH_3$ (TS 2)	11.77	16.14	-1138.24	2.84	$2.63 \cdot 10^{10}$		
$CH_2{=}CHC(NO_2)O\cdot CH_3$ (TS 3)	14.27	18.20	-1158.70	3.19	$1.29 \cdot 10^{10}$		
$CH_2{=}CHC(NO_2)O\cdot CH_3$ (TS 4)	16.38	18.44	-1235.82	3.90	$1.43 \cdot 10^{10}$	$5.34 \cdot 10^{10}$	-120.16

Table S4. ωB97X-D3/jun-cc-pV(T+d)Z level computational results for the kinetics of α-NO_2 ejection from alkoxy radicals at $T = 298.15$ K. The TS are numbered from lowest to highest $G_i^\ddagger$. $E_i^\ddagger$ is the zero-point corrected activation barrier of each transition state relative to the reactant conformer that connects to it (In other words, the forward barrier value used in the Eckart tunneling coefficient calculation). ω_i is the imaginary vibrational frequency of the TS mode, and ΔH is the heat of the reaction.

Based on the results in Table S4, the α-NO_2 ejection is not quite as fast as the 'arbitrarily high' 10^{12} s^{-1} assigned to it by GECKO-A. Nevertheless the calculated MC-TST rates suggest that the reaction is indeed fast enough to sit firmly inside the 'competitive in-complex' range. Furthermore, for the $(CH_3)_2C(NO_2)O\cdot$ and $CH_2{=}CHC(NO_2)O\cdot CH_3$ systems the rate is rapid enough to very likely be the dominant $^3(\text{RO}\ldots\text{OR})$ reaction channel in most cases, barring complexes with exceptionally fast ISC rates or extremely fast Exo-β-scission rates. In other words, the discussion on accretion product inhibition in Sect. 3.3 in the main text is largely speaking accurate: Peroxy radicals with α-NO_2 substituents, to the extent that they form, are not a source of accretion products.

The important caveat to this conclusion is that the DFT-level energetics might not be fully accurate. DLPNO-CCSD(T)-F12 single-point corrections for the electronic energy were attempted, but the ROHF reference wavefunction failed to converge for the transition states even after 1000 SCF cycles. The explanation for this is likely the high delocalisation of the spin density. In the Mulliken population analysis of the transition state structure, approximately $60-65$ % (depending on the system) of the spin density was located at the alkoxy oxygen and the rest distributed $10-15$ % each between the three atoms in the NO_2 leaving group. This leads us to suspect that the transition state has a highly multi-configuration character, meaning that post-DFT electronic energy corrections likely must be calculated using a multi-reference method. However, calculations like these are well beyond the scope of this work, as our main focus is in applying Structure-activity relationship results to in-complex RO reactions. The ωB97X-D3/jun-cc-pV(T+d)Z results are enough to conclude that the reaction likely occurs.

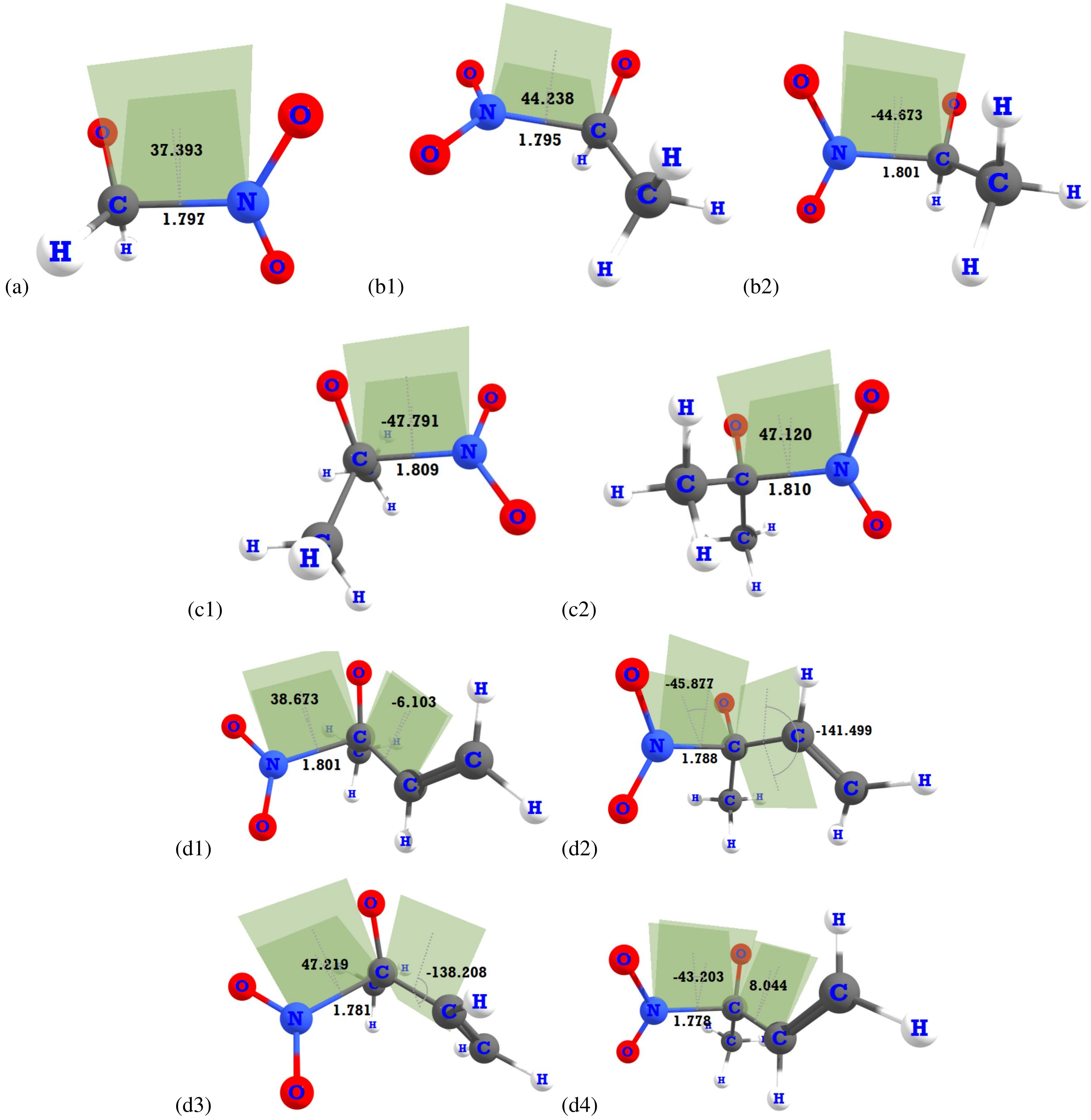
(a) (b1) (b2)

(c1) (c2)

(d1) (d2)

(d3) (d4)

Figure S5. Molecular geometries of the transition states, with the most important geometric parameters, i.e. the CN bond length, the $\angle(\mathrm{CO}\cdot,\mathrm{NO})$ dihedral angle, and the $\angle(\mathrm{CO}\cdot,\mathrm{C{=}C})$ dihedral angle, shown. (a) $CH_2(NO_2)O\cdot$ (b) $CH_3CH(NO_2)O\cdot$ TS 1 and 2 (c) $(CH_3)_2C(NO_2)O\cdot$ TS 1 and 2 (d) $CH_2{=}CHC(NO_2)O\cdot CH_3$ TS 1-4.

S4 Accuracy of Nannoolal Vapour Pressures

In a comparison study of different group contribution methods and computational methods for determining the saturation vapour pressures (p_{Sat}) of α-pinene derived oxidation products (Kurtén et al., 2016), unphysical values and odd trends were reported for the highly oxidized products in general and the (peroxide) accretion products in particular. Potential causes of these oddities were investigated by reproducing the molecules from that study in the Gecko structural format and comparing the article's reported p_{Sat}-values with those determined using GECKO-A's internal SIMPOL (Pankow and Asher, 2008) and Nannoolal (Nannoolal et al., 2004, 2008; Compernolle et al., 2010) p_{Sat} calculators, which have already proven themselves against experimental aerosol growth rates. (Barley and McFiggans, 2010; Valorso et al., 2011) The results are presented in Table S5. These results show that GECKO-A's native implementation produces different results from that of UManSysProp, (Topping) which was used by Kurtén et al. (2016), especially for the three C_{20} accretion products. In addition, the results are generally more in line with the other group contribution models. This suggests that the reported unphysical trends are due to UManSysProp's implementation of the Nannoolal model, not due to the model itself.

Name	n_{OOH}	COSMO^a	Nan.^{a}	EVAP.^{a}	SIM.^{a}	Nan.^{b}	SIM.^{b}
$C_{10}H_{16}O_4$-iso1	1	-6.0	-5.7	-6.0	-7.1	-7.0	-7.1
$C_{10}H_{16}O_4$-iso2	1	-7.3	-5.5	-5.8	-7.1	-6.7	-7.1
$C_{10}H_{16}O_4$-iso3	1	-6.7	-6.1	-6.1	-7.1	-6.8	-7.1
$C_{10}H_{16}O_5$	1	-6.0	-7.2	-7.7	-8.0	-8.4	-8.0
$C_{10}H_{16}O_6$-iso1	1	-5.5	-8.0	-8.0	-8.9	-9.1	-8.9
$C_{10}H_{16}O_6$-iso2	1	-8.1	-10.1	-10.5	-10.2	-11.4	-10.2
$C_{10}H_{16}O_7$-iso1	2	-5.9	-9.4	-9.5	-9.1	-10.7	-9.1
$C_{10}H_{16}O_7$-iso2	1	-8.8	-13.6	-12.0	-12.4	-13.9	-12.4
$C_{10}H_{16}O_8$-iso1	2	-8.0	-15.3	-13.7	-12.7	-15.7	-12.7
$C_{10}H_{16}O_8$-iso2	2	-6.4	-12.7	-11.0	-11.3	-13.0	-11.3
$C_{10}H_{16}O_8$-iso3	2	-8.1	-8.7	-9.2	-8.6	-9.6	-8.6
$C_{10}H_{16}O_9$	3	-6.6	-14.4	-12.7	-11.6	-14.7	-11.6
$C_{10}H_{16}O_{10}$	3	-7.5	-13.4	-12.7	-11.1	-13.4	-11.1
$C_{20}H_{30}O_{10}$-iso1	0	-11.9	-9.1	-13.7	-17.0	-17.4	-17.1
$C_{20}H_{30}O_{10}$-iso2	1	-12.2	-10.6	-14.9	-15.1	-16.7	-16.0
$C_{20}H_{30}O_{12}$	2	-10.1	-11.6	-16.7	-17.5	-20.7	-17.6

Table S5. $\log_{10}(p_{Sat}\ (\mathrm{atm}))$ values predicted using different vapour pressure models. Nan: Nannoolal, SIM: SIMPOL, EVAP: EVAPORATION (Compernolle et al., 2011)

[a] Value from Kurtén et al. (2016). COSMO refers here specifically to the single conformer BP/TZVPD-FINE results, the most accurate computation performed for all 16 molecules.

[b] This work, using GECKO-A's vapour pressure calculators. (Valorso et al., 2011)

S5 Sensitivity Analysis of the Yield filter

To analyse the sensitivity of the $RO_2 + RO_2$ recombination yield cutoff, a simplified version of the GECKO-AP code was made that only calculated $y_{\mathrm{RO_2RO_2}}$ for the list of RO_2's without generating product pathways. As a model precursor molecule for the sensitivity analysis, α-pinene was chosen due to being included in two of the three datasets, and due to having a suitably representative diversity of oxidation pathways. The RO_2's were generated up to the 5th generation with very low cutoff. ($y_c = 0.0005$) This resulted in a list of 32 199 RO_2's and 644 325 RO_2 pairs. Each radical was assigned a generation using the same method described in Sect. 2.2.2 of the main text, and the pairs were categorized based on the generation combination of the two radicals. Figure S6 shows the number of $RO_2 + RO_2$ pairs per generation where $y_{\mathrm{RO_2RO_2}}$ lies above a certain yield cutoff. As seen in Figure S6 (b), higher generation pairings dominate the statistics at low yield cutoffs but are filtered out at higher ones. The latter is somewhat more desirable as we know that the theoretical maximum yields we are using to filter products are closer to reality in the initial generations. Based on the same graph, the range around 0.004-0.01 is where the recombination products of 3rd and 4th generation RO_2's with 2nd and 1st generation radicals start outnumbering the reactions where both radials are from the 3rd or 4th generation. This was thus treated as a good cutoff range for the DTA dataset where products were generated up to the 4th generation. For the Terpene dataset, managing the large amount of overall products was considered a more important criteria for the cutoff. Here 0.0025-0.004 was deemed a good cutoff range as here around 15-25 % of the 23 442 1st and 2nd generation RO_2 pairs remained. For the single generation β-caryophyllene dataset the cutoff 0.001 was deemed suitable, as this included the majority (251/404) of the 1st generation RO_2 pairs in this test run while still filtering out the least likely ones.

The removal of reaction pathways requiring simultaneously high concentrations of OH and NO_3 described in Sect. 2.2.2 of the main text was not performed here, as the necessary data curation is more involved. However, it is clear that this filtering criteria disproportional removed higher generation $RO_2 + RO_2$ pairs, as every generation by definition adds one more VOC + Oxidant step to the total mechanism. As such, this additional filtering step can be seen as yet another way to remove higher generation products whose importance is overestimated due to the usage of the theoretical maximum yields as $RO_2 + RO_2$ filtering criteria.

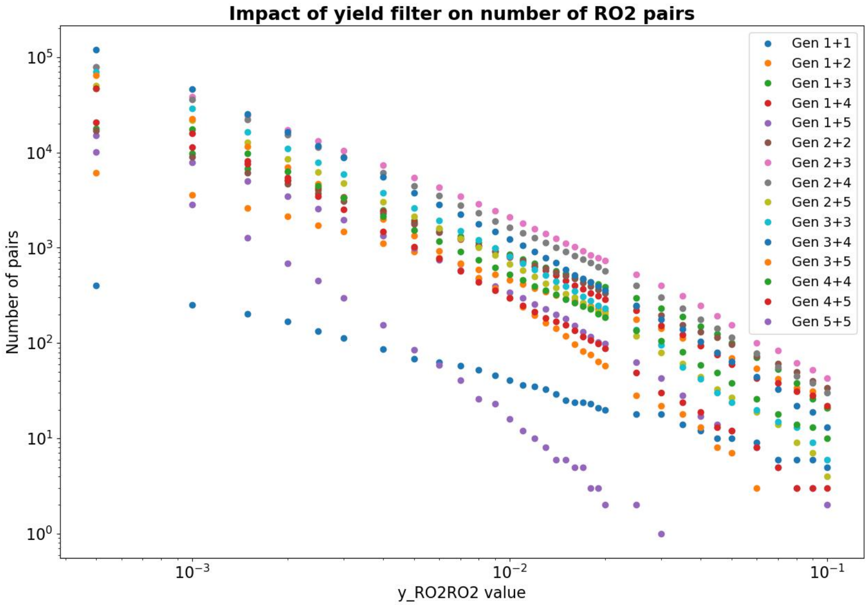

(a)

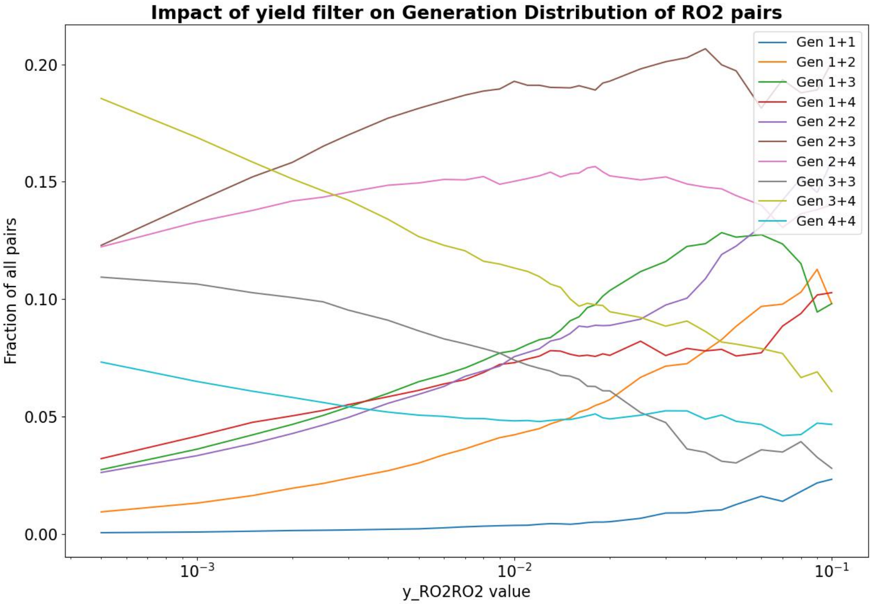

(b)

Figure S6. (a) The number of RO_2 pairs by generation as a function of $y_{RO_2RO_2}$ cutoff. As seen in the graph, higher generation products are filtered more heavily due to generally having lower theoretical maximum yields. (b) The number of RO_2 pairs by generation as a fraction of total number of RO_2 pairs. The 5th generation products are not shown to avoid clutter.

S6 Vapour Pressure Visualisations

S6.1 DTA Dataset

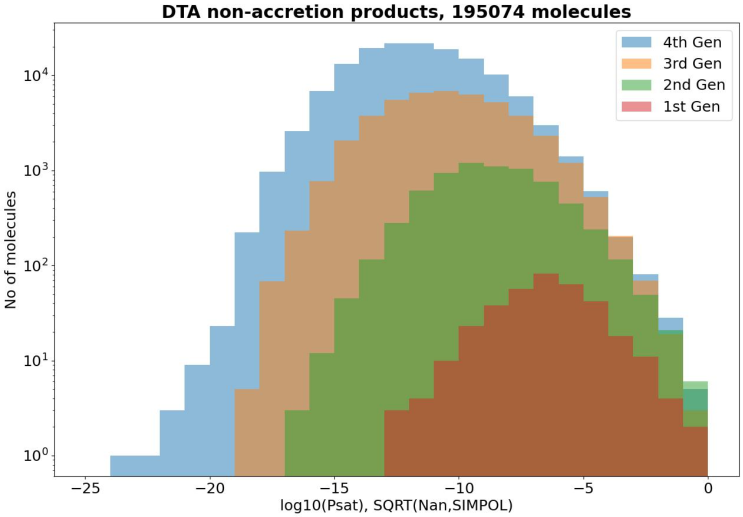

Figure S7. Saturation vapour pressure distribution of non-accretion products in the DTA Dataset.

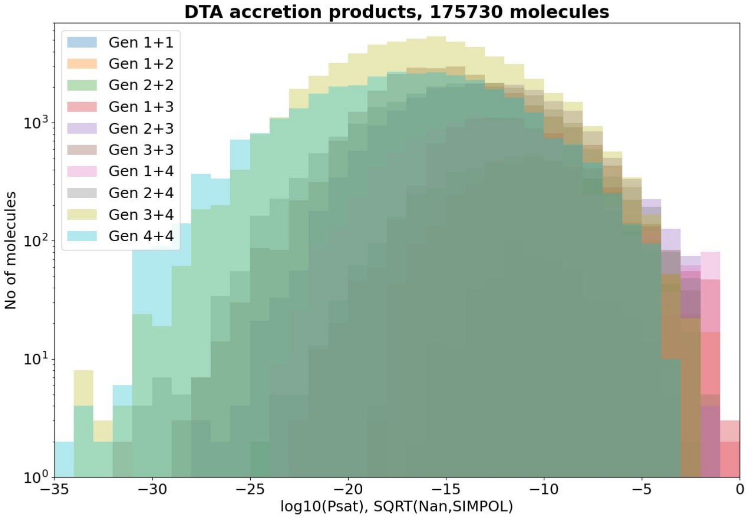

Figure S8. Saturation vapour pressure distribution of accretion products in the DTA Dataset.

S6.2 Terpene Dataset

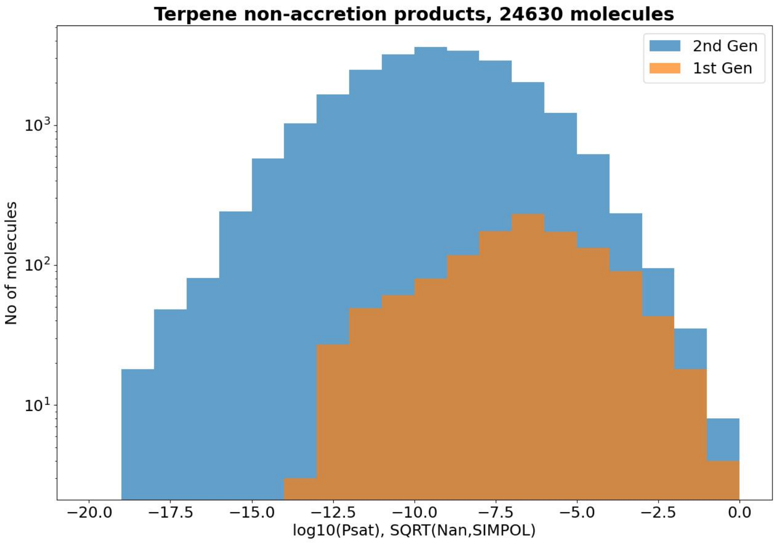

Figure S9. Saturation vapour pressure distribution of non-accretion products in the Terpene Dataset.

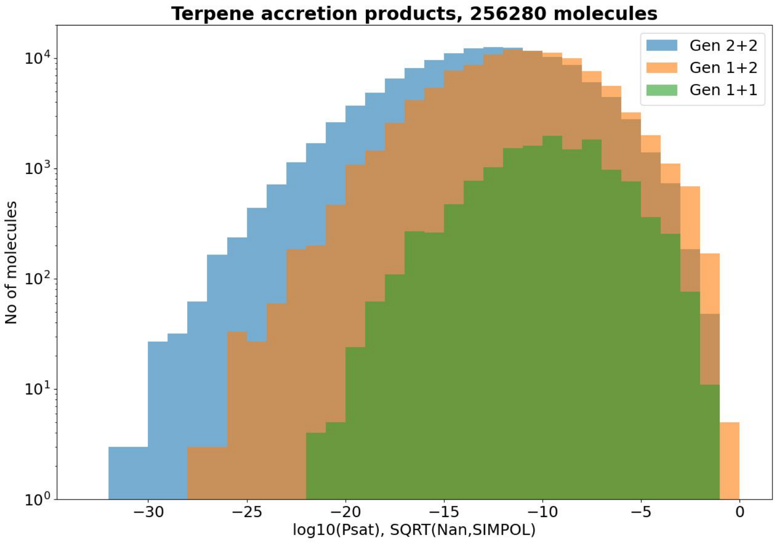

Figure S10. Saturation vapour pressure distribution of accretion products in the Terpene Dataset.

S6.3 β-caryophyllene Dataset

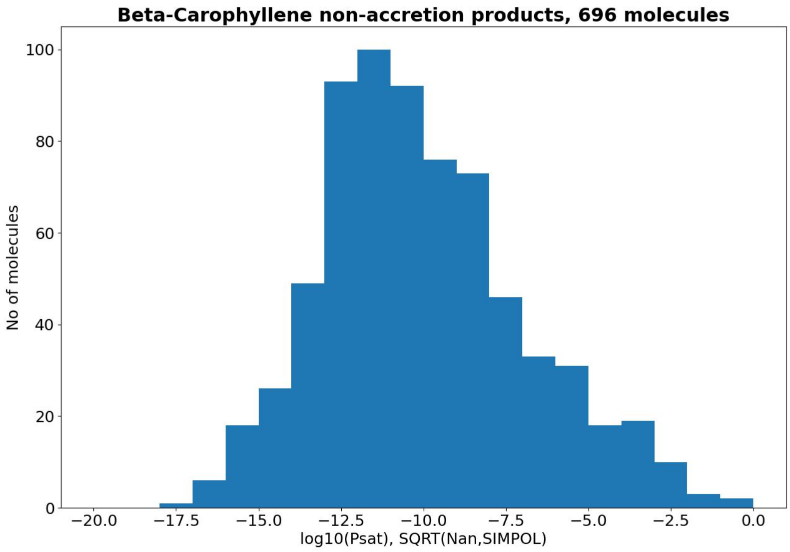

Figure S11. Saturation vapour pressure distribution of β-caryophyllene non-accretion products.

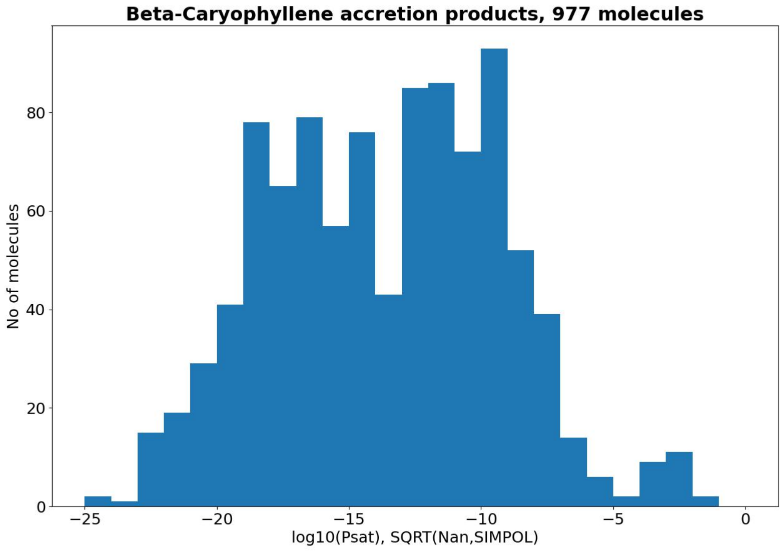

Figure S12. Saturation vapour pressure distribution of β-caryophyllene accretion products.

S7 Tables on distributions of accretion product properties

In Sect. 3.4 of the main text we discussed our main observations from the data when analysing which $RO_2 + RO_2$ reaction channels lead to low-volatility products. In this section, the same topic is analysed more systematically with generation-by-generation tables on the numbers, estimated $RO_2 + RO_2$ branching ratios, and ELVOC ($p_{Sat} < 10^{-13}$ atm) percentages.

S7.1 Distribution by Reaction Channel

The distribution of accretion products by in-complex reaction channel is presented for the Terpene dataset in Table S6, for the β-caryophyllene dataset (together with the distribution by VOC oxidant, explained properly in Sect. S7.3) in Table S7, and for the DTA dataset in Table S8.

Molecules	ISC	Exo-β	Endo-β	H-Shift	All
Gen 1+1	5 958	5 602	1 989	313	13 862
Gen 1+2	51 731	43 784	11 193	1 260	107 968
Gen 2+2	71 896	51 899	9 612	1 043	134 450
$\langle$Branching$\rangle$	ISC	Exo-β	Endo-β	H-Shift	All
Gen 1+1	38.5 %	66.6 %	72.7 %	1.9 %	53.9 %
Gen 1+2	37.2 %	66.6 %	73.6 %	2.5 %	52.5 %
Gen 2+2	36.0 %	69.5 %	73.7 %	3.0 %	51.4 %
$p_{\mathrm{Sat}} < 10^{-13}$	ISC	Exo-β	Endo-β	H-Shift	All
Gen 1+1	18.0 %	2.8 %	32.8 %	33.9 %	14.3 %
Gen 1+2	40.2 %	10.2 %	53.9 %	57.9 %	29.7 %
Gen 2+2	62.2 %	23.0 %	62.5 %	73.0 %	47.2 %

Table S6. The amounts, average branching ratios,, and p_{Sat} distributions of the accretion products by reaction channel for the Terpene dataset.

Channel	ISC	Exo-β	Endo-β	H-Shift
$\langle$Branching$\rangle$	43.0 %	67.8 %	79.1 %	1.5 %
$p_{\mathrm{Sat}} < 10^{-13}$	66.0 %	27.0 %	68.6 %	86.2 %
Oxidant	OH	O_3	NO_3	All
Molecules	54	461	12	977
$p_{\mathrm{Sat}} < 10^{-13}$	68.5 %	46.2 %	41.7 %	51.8 %

Table S7. The amounts, average branching ratios, and p_{Sat} distributions of the accretion products by reaction channel and oxidant for the β-caryophyllene dataset.

Molecules	ISC	Exo-β	Endo-β	H-Shift	All
Gen 1+1	213	45	254	22	534
Gen 1+2	1 647	987	1 329	93	4 056
Gen 2+2	2 260	1 615	934	61	4 870
Gen 1+3	3 445	1 595	3 738	123	8 901
Gen 2+3	9 446	5 933	6 511	207	22 097
Gen 3+3	10 599	5 709	10 898	194	27 400
Gen 1+4	4 018	2 020	4 008	140	10 186
Gen 2+4	10 818	6 794	5 869	215	23 696
Gen 3+4	23 100	13 345	21 144	402	57 991
Gen 4+4	14 287	9 043	9 713	103	33 146
$\langle$Branching$\rangle$	ISC	Exo-β	Endo-β	H-Shift	All
Gen 1+1	45.4 %	53.4 %	60.7 %	5.6 %	52.7 %
Gen 1+2	35.2 %	69.0 %	59.7 %	5.3 %	50.8 %
Gen 2+2	35.6 %	73.5 %	66.0 %	5.6 %	53.6 %
Gen 1+3	31.4 %	62.6 %	57.5 %	5.5 %	47.6 %
Gen 2+3	31.1 %	69.5 %	59.8 %	5.0 %	49.6 %
Gen 3+3	25.1 %	66.6 %	55.4 %	5.4 %	45.7 %
Gen 1+4	33.4 %	68.1 %	58.9 %	5.4 %	49.9 %
Gen 2+4	38.4 %	76.1 %	65.0 %	5.3 %	55.5 %
Gen 3+4	31.7 %	72.3 %	60.2 %	4.9 %	51.3 %
Gen 4+4	40.5 %	77.4 %	65.5 %	4.5 %	57.8 %
$p_{\mathrm{Sat}} < 10^{-13}$	ISC	Exo-β	Endo-β	H-Shift	All
Gen 1+1	10.8 %	2.2 %	14.2 %	54.5 %	13.5 %
Gen 1+2	15.5 %	4.2 %	36.8 %	43.0 %	20.3 %
Gen 2+2	35.2 %	20.6 %	56.5 %	52.5 %	34.7 %
Gen 1+3	27.1 %	4.5 %	57.9 %	64.2 %	36.5 %
Gen 2+3	49.2 %	22.0 %	78.1 %	87.9 %	50.8 %
Gen 3+3	65.2 %	27.1 %	89.9 %	96.4 %	67.3 %
Gen 1+4	45.7 %	9.3 %	77.7 %	89.3 %	51.7 %
Gen 2+4	60.6 %	29.7 %	89.0 %	94.9 %	59.1 %
Gen 3+4	77.1 %	37.3 %	96.0 %	99.5 %	75.0 %
Gen 4+4	86.1 %	45.8 %	97.8 %	100 %	78.6 %

Table S8. The amounts, average branching ratios, and p_{Sat} distributions of the accretion products by in-complex reaction channel for the DTA dataset.

Here we largely see the same trends already discussed in the main article. Endocyclic β-scission products have generally the lowest volatilities, apart from H-shift products, which have even lower volatilities but also low yields.

S7.2 Distribution by Precursor Molecule

The accretion products are categorized by precursor molecule in Table S10 for the DTA dataset and in Table S11 for the Terpene dataset. As the RO_2 are not limited to only reacting with RO_2 formed from other precursor molecules (in the code or in reality), we group the products both exclusively (e.g. both RO_2 must be derived from Isoprene) and inclusively (e.g. Either RO_2 can be derived from Isoprene).

Molecules	B. Iso	B. α-pin	B. β-pin	B. Lim	B. β-oci	B. Sabi	B. Δ-Car	B. Myr
Gen 1+1	414	420	618	1 988	492	465	190	968
Gen 1+2	1 749	3 875	5 568	16 814	4 013	3 134	2 121	7 903
Gen 2+2	1 111	4 760	5 380	14 594	3 707	2 208	2 820	7 444
$p_{\mathrm{Sat}} < 10^{-13}$	B. Iso	B. α-pin	B. β-pin	B. Lim	B. β-oci	B. Sabi	B. Δ-Car	B. Myr
Gen 1+1	1.0 %	7.9 %	21.4 %	3.8 %	1.4 %	21.5 %	0.0 %	6.5 %
Gen 1+2	5.8 %	15.0 %	30.6 %	20.6 %	9.8 %	24.5 %	10.0 %	19.3 %
Gen 2+2	15.3 %	33.7 %	48.5 %	34.5 %	22.7 %	37.8 %	22.1 %	37.3 %
Molecules	E. Iso	E. α-pin	E. β-pin	E. Lim	E. β-oci	E. Sabi	E. Δ-Car	E. Myr
Gen 1+1	4 864	4 183	5 265	9 130	5 189	4 255	3 641	6 539
Gen 1+2	37 660	38 704	44 901	70 370	42 739	35 532	34 267	53 399
Gen 2+2	26 856	49 240	50 115	72 661	43 203	32 829	40 175	57 831
$p_{\mathrm{Sat}} < 10^{-13}$	E. Iso	E. α-pin	E. β-pin	E. Lim	E. β-oci	E. Sabi	E. Δ-Car	E. Myr
Gen 1+1	6.8 %	11.9 %	17.8 %	10.0 %	7.0 %	17.7 %	7.4 %	10.4 %
Gen 1+2	16.8 %	22.1 %	28.7 %	25.1 %	19.0 %	24.1 %	18.5 %	23.0 %
Gen 2+2	30.3 %	41.3 %	47.5 %	41.5 %	34.1 %	40.1 %	35.1 %	41.3 %

Table S9. The amounts and p_{Sat} distributions of the accretion products by peroxy radical precursor molecules. 'B.' and 'E.' are short for 'Both' and 'Either', respectively.

Molecules	B. Dec	B. Tol	B. α-pin	E. Dec	E. Tol	E. α-pin
Gen 1+1	25	124	93	222	457	367
Gen 1+2	430	974	1 110	1 868	3 369	3 212
Gen 2+2	169	1 061	2 368	1 484	3 494	4 431
Gen 1+3	248	2 695	2 054	3 110	7 937	6 419
Gen 2+3	335	6 658	7 270	5 816	18 205	17 629
Gen 3+3	259	10 436	4 766	5 436	24 812	19 074
Gen 1+4	110	4 585	1 623	3 167	9 713	6 367
Gen 2+4	47	9 159	4 609	4 860	21 698	17 421
Gen 3+4	51	28 520	5 011	6 729	55 923	33 387
Gen 4+4	0	19 785	1 525	1 412	32 890	14 607
$p_{\mathrm{Sat}} < 10^{-13}$	B. Dec	B. Tol	B. α-pin	E. Dec	E. Tol	E. α-pin
Gen 1+1	0.0 %	18.5 %	8.6 %	5.9 %	13.1 %	11.4 %
Gen 1+2	0.0 %	20.8 %	17.0 %	6.3 %	18.0 %	18.0 %
Gen 2+2	0.0 %	28.2 %	33.2 %	11.9 %	26.6 %	33.6 %
Gen 1+3	0.0 %	36.3 %	19.6 %	15.2 %	36.5 %	31.4 %
Gen 2+3	1.5 %	50.0 %	37.3 %	25.2 %	50.0 %	46.5 %
Gen 3+3	3.1 %	75.1 %	43.1 %	28.8 %	69.1 %	62.9 %
Gen 1+4	0.0 %	54.4 %	23.8 %	24.9 %	51.3 %	43.0 %
Gen 2+4	0.0 %	59.9 %	45.4 %	33.9 %	58.2 %	56.1 %
Gen 3+4	5.9 %	81.9 %	51.7 %	44.3 %	75.3 %	68.9 %
Gen 4+4	0.0 %	84.3 %	48.8 %	38.7 %	78.5 %	71.8 %

Table S10. The amounts and p_{Sat} distributions distributions of the accretion products by peroxy radical precursor molecules. 'B.' and 'E.' are short for 'Both' and 'Either', respectively.

The main trend observed when categorizing the accretion products by precursor molecule were already discussed in the main article.

S7.3 Distribution by VOC Oxidant

The accretion products are categorized by required oxidants in Table S12. This is a somewhat fuzzy categorization, as higher generation radicals need multiple VOC + Oxidant steps to form, and as the two RO_2 forming the reactive pair have different formation pathways. Due to this complexity the following tables were made with a simple but consistent criteria: Accretion product where both reactant RO_2 have OH oxidation at some point in their formation mechanism are classified as OH-derived. The results are presented for the Terpene dataset in Table S11 and for the DTA dataset in Table S12.

Molecules	OH	O_3	NO_3	All
Gen 1+1	6 280	2 569	2 735	13 862
Gen 1+2	51 488	23 710	31 012	107 968
Gen 2+2	60 490	24 578	58 201	134 450
$p_{\text{Sat}} < 10^{-13}$	OH	O_3	NO_3	All
Gen 1+1	11.7 %	4.6 %	22.0 %	14.3 %
Gen 1+2	23.6 %	16.7 %	36.1 %	29.7 %
Gen 2+2	37.1 %	31.7 %	57.1 %	47.2 %

Table S11. The amounts and p_{Sat} distributions of the accretion products by VOC oxidant in the Terpene dataset.

These results from these tables are largely unsurprising: OH oxidation produces both the most diverse set of accretion products, due to producing the most diverse set of radicals, and generally also the lowest vapour pressures, due to OH addition being a more common reaction channel than NO_3 addition.

Molecules	OH	O_3	NO_3	All
Gen 1+1	326	15	18	534
Gen 1+2	3 211	290	490	4 056
Gen 2+2	4 025	986	1 573	4 870
Gen 1+3	7 208	392	495	8 901
Gen 2+3	20 224	2 922	4 171	22 097
Gen 3+3	26 482	1 489	2 247	27 400
Gen 1+4	8 508	419	455	10 186
Gen 2+4	21 965	3 359	3 775	23 696
Gen 3+4	55 899	2 882	4 880	57 991
Gen 4+4	31 924	1 500	2 950	33 146
$p_{\text{Sat}} < 10^{-13}$	OH	O_3	NO_3	All
Gen 1+1	13.8 %	0.0 %	0.0 %	13.5 %
Gen 1+2	18.4 %	23.4 %	15.9 %	20.3 %
Gen 2+2	31.9 %	36.5 %	38.3 %	34.7 %
Gen 1+3	33.4 %	37.2 %	17.6 %	36.5 %
Gen 2+3	50.8 %	45.7 %	43.5 %	50.8 %
Gen 3+3	67.8 %	55.7 %	51.7 %	67.3 %
Gen 1+4	50.0 %	45.6 %	41.5 %	51.7 %
Gen 2+4	59.3 %	52.0 %	50.6 %	59.1 %
Gen 3+4	75.7 %	56.6 %	53.6 %	75.0 %
Gen 4+4	79.5 %	57.9 %	54.7 %	78.6 %

Table S12. The amounts and vapour pressure distributions of the accretion products by VOC oxidant.

S7.4 Distribution by RO_2 class

Finally, the only variable in the data we haven't looked at is the RO_2 rate class. In the tables below, all the accretion products where one of the two RO_2 belongs to a specific rate class and generation are grouped together. $CH_3C(O)O_2$ is listed separately, as it is the only $RC(O)O_2$ for which we did not apply the smaller recombination yield factor due to an assumed autoxidation sink. This is presented in Table S13 for the DTA dataset and Table S14 for the Terpene and β-cayophyllene datasets.

Molecules	1	3	4	5	7	8	9	$CH_3C(O)O_2$
Gen 1	135	405	4 234	192	4 351	9 221	815	4 799
Gen 2	355	882	3 508	31	22 203	25 313	6 192	0
Gen 3	436	3 650	7 101	1 078	43 165	75 945	4 808	0
Gen 4	155	2 376	7 514	567	56 529	75 914	7 940	0
$p_{\mathrm{Sat}} < 10^{-13}$	1	3	4	5	7	8	9	$CH_3C(O)O_2$
Gen 1	20.0 %	43.5 %	39.7 %	27.1 %	44.8 %	51.1 %	56.3 %	8.4 %
Gen 2	20.6 %	43.3 %	33.1 %	54.8 %	54.7 %	54.2 %	26.0 %	-
Gen 3	39.4 %	36.5 %	68.4 %	83.5 %	57.7 %	72.6 %	42.8 %	-
Gen 4	19.4 %	45.5 %	58.3 %	97.7 %	76.0 %	73.3 %	53.3 %	-

Table S13. The amounts and vapour pressure distributions of the accretion products by RO_2 rate class in the DTA dataset.

The main observation from these tables is a fully expected result: The list of RO_2 pairs is dominated by RO_2 at the faster end of the recombination rate scale. Acyl peroxy radicals (rate class 9) are not quite as dominant, but that is likely fully explained by the fact that we scaled down their recombination yields due to the assumed autoxidation sink. The results for $CH_3C(O)O_2$ are also interesting but expected: The number of RO_2 pairs including it is large, but they typically do not have low vapour pressures, presumably due to their lower-than-average size. These results underline that there are always two factors to which RO_2 pairs contribute the most to ELVOC formation: recombination rates and low-volatility products with large branching ratios. $CH_3C(O)O_2 + RO_2$ pairs fill the first criteria, but often not the second.

Molecules	1	3	4	5	7	8	9	$CH_3C(O)O_2$
Gen 1	895	9 299	9 357	9 946	44 924	48 725	3 825	5 888
Gen 2	2 725	26 270	14 781	13 439	145 346	117 729	26 816	0
β-Car.	56	145	145	180	618	338	92	216
$p_{\mathrm{Sat}} < 10^{-13}$	1	3	4	5	7	8	9	$CH_3C(O)O_2$
Gen 1	29.2 %	32.1 %	43.9 %	23.0 %	27.6 %	26.2 %	18.1 %	3.7 %
Gen 2	36.1 %	45.7 %	39.5 %	45.6 %	41.3 %	44.8 %	30.3 %	-
β-Car.	19.6 %	62.8 %	55.9 %	57.2 %	58.9 %	52.1 %	71.7 %	6.5 %

Table S14. The amounts and vapour pressure distributions of the accretion products by RO_2 rate class in the Terpene and β-caryophyllene datasets.

S8 Technical Details on Estimation of Atmospheric Concentrations

$$\frac{\mathrm{d}c}{\mathrm{d}t} = Sources - Sinks \cdot c \approx 0 \implies c \approx \frac{Sources}{Sinks} \tag{5}$$

As discussed in the main text, Isoprene-RO_2 concentrations were estimated by solving the kinetic steady-state equations derived from the generated GECKO-A mechanism. The concentrations of O_3, OH, HO_2, NO, NO_2, and NO_3 were optimized for conditions where $RO_2{}^{+}RO_2$ was expected to be relatively important, using Kenagy et al. (2024) and Bey et al. (1997) as reference. Below are the constant concentrations used for CH_4, CO, CH_2O, CH_3OH and H_2O used for deriving the radicals concentrations:

Reactant	Daytime	Nighttime
H_2O	$5.38{\cdot}10^{17}$	$5.38{\cdot}10^{17}$
CH_4	$4.31{\cdot}10^{13}$	$4.31{\cdot}10^{13}$
CO	$2.45{\cdot}10^{12}$	$2.45{\cdot}10^{12}$
CH_2O	$2.45{\cdot}10^{10}$	$2.45{\cdot}10^{10}$
CH_3OH	$2.45{\cdot}10^{10}$	$2.45{\cdot}10^{10}$
O_3	$9.85{\cdot}10^{11}$	$9.85{\cdot}10^{11}$
Isoprene	$1.0{\cdot}10^{11}$	$1.0{\cdot}10^{10}$
OH	$7.70{\cdot}10^{6}$	$1.90{\cdot}10^{4}$
HO_2	$6.7{\cdot}10^{8}$	$6.2{\cdot}10^{6}$
NO	$1.7{\cdot}10^{8}$	$5.8{\cdot}10^{5}$
NO_2	$5.75{\cdot}10^{8}$	$6.0{\cdot}10^{8}$
NO_3	$1.0{\cdot}10^{5}$	$8.45{\cdot}10^{7}$
CH_3O_2	$4.499{\cdot}10^{8}$	$1.200{\cdot}10^{8}$
CH_3O_2	$1.822{\cdot}10^{8}$	$3.904{\cdot}10^{7}$

Table S15. Concentrations of all the relevant bimolecular reactants for the concentrations in unit $\mathrm{molecule\ cm^{-3}}$. Values above the first horizontal line were treated as constants used to solve the steady-state equations. Values between the lines were received as results of the steady-state equations with no Isoprene present, whereas the CH_3O_2 value below the line was the result with Isoprene present. The concentration of H_2O corresponds to 70 % relative humidity at 298 K.

The CH_3O_2 concentration was received as a side product, as its' atmospheric main source is $CH_4 + OH$. Unlike the other reactants in the table, this was not treated as a constant when solving the Isoprene-RO_2 equations, as the Isoprene mechanism included both secondary sources ($CH_3C(O)O_2 + \text{Reactant} \longrightarrow CH_3C(O)O \longrightarrow CH_3 + CO_2$, $CH_3 + O_2 \longrightarrow CH_3O_2$) and additional sinks ($CH_3O_2 + RO_2$).

The steady-state equations were solved in multiple steps: First, guess concentrations of the RO_2 formed from primary Isoprene $+ OH/O_3/NO_3$ reactions were calculated using the constant formation rates and using only the reactions with inorganic radicals (OH, HO_2, NO, NO_2 ($k_{RO2NO2} = 0$ for all but $RC(O)O_2$), NO_3) as sinks. Second, the steady-state concentrations of all 1st generation RO_2, including those indirectly formed from reactions of the primary radicals, were solved by iteratively calculating source terms and sinks as a function of the set of RO_2 concentrations, followed by updated concentrations as a function of the new source and sink terms. Here unimolecular decomposition of peroxyacetyl nitrates ($RC(O)OONO_2$) was included as a source of $RC(O)O_2$. Iterations were continued until all concentrations changed by less than 0.1 % from the previous iteration. Third, the converged RO_2 concentrations were used to calculate formation rates for the 1st generation closed-shell products, along with sink rates using their respective $OH/O_3/NO_3$ reaction rate coefficients and photolysis rates in the mechanism. As a final step, the same procedure was followed for the 2nd generation radicals with the concentrations of all 1st generation RO_2 (including CH_3O_2) and closed-shell species also treated as variables. As previously, the equations were treated as converged when all concentrations changed less than 0.1 % from the previous iteration. A few minor modifications were made to the standard GECKO-A RO_2 scheme presented by Jenkin et al. (2019) for the purposes of this simulation: First, $RO_2 + RO_2$ reactions were purely treated as a sink, since our hypothesis is that accretion product formation out-competes both the dissociation and bimolecular H-shift channels for sufficiently complex RO_2 pairs. Second, as the first modification may result in an underestimation of radical recycling from RO_2 reactions, $RO_2 + OH$ reactions were treated explicitly with the assumption that these uniformly produce $RO + HO_2$ for all non-acyl RO_2 ($RC(O)O_2 + OH$ on the other hand were treated as a sink due to lack of information of the products). A dataset of the resulting set of RO_2 concentrations is found in the Zenodo repository together with the accretion product datasets.

Class	Description	c (Day)	c (Night)
1	unsubstituted tert-RO_2	0	0
2	i-$C_3H_7O_2$	0	0
3	tert-RO_2 with α- or β- O or N	$2.902 \cdot 10^8$ molecule cm^{-3}	$6.821 \cdot 10^7$ molecule cm^{-3}
4	$C_2H_5O_2$; unsubstituted sec-RO_2;	0	0
5	tert-RO_2 with α- or β- O or N and allylic or β-aryl group	$1.108 \cdot 10^9$ molecule cm^{-3}	$1.098 \cdot 10^9$ molecule cm^{-3}
6	CH_3O_2	$1.822{\cdot}10^8$ molecule cm^{-3}	$3.904{\cdot}10^7$ molecule cm^{-3}
7	unsubstituted prim-RO_2; sec-RO_2 with α- or β- O or N	$9.240 \cdot 10^8$ molecule cm^{-3}	$7.909 \cdot 10^7$ molecule cm^{-3}
8	prim-RO_2 with α- or β- O or N; sec-RO_2 with α- or β- O or N and allylic or β-aryl group	$1.353 \cdot 10^9$ molecule cm^{-3}	$9.620 \cdot 10^6$ molecule cm^{-3}
9	$RC(O)O_2$	$2.233 \cdot 10^7$ molecule cm^{-3}	$4.596 \cdot 10^6$ molecule cm^{-3}

Table S16. Concentrations of the Isoprene-RO_2 by Jenkin rate class.

To provide more context to the table presented in the main text, the RO_2 concentration is split into Jenkin rate classes in Table S16. As we seen, the most notable difference between day and night is in the total concentration of rate class 8, which is dominated by the primary RO_2 formed from Isoprene + OH. The concentrations of other classes were depressed to a lesser extent, likely largely due to the lower Isoprene concentration, the major exception being rate class 5, as this class includes the major RO_2 forming from Isoprene + NO_3, $CH_3C(OO\cdot)(CH_2ONO_2)CH{=}CH_2$. This observation adds further nuance to our claim that Isoprene-RO_2 typically having higher-than-average $RO_2 + RO_2$ rates. The claim is mainly true at daytime when OH concentrations are relatively high.

In Figure S13, vapour pressure bubble plots similar to those presented in the main article are shown weighted by the formation rates of the accretion products, $k_{\mathrm{RO_2RO_2},\alpha+\beta}[\alpha][\beta] \times \mathrm{Branching}$, where $[\alpha]$ and $[\beta]$ represent the steady-state concentrations of the radicals solved from the steady-state equations, and $\mathrm{Branching}$ is branching ratio. As we do not have estimates of reaction rates for the accretion products, this is our best proxy of their concentrations.

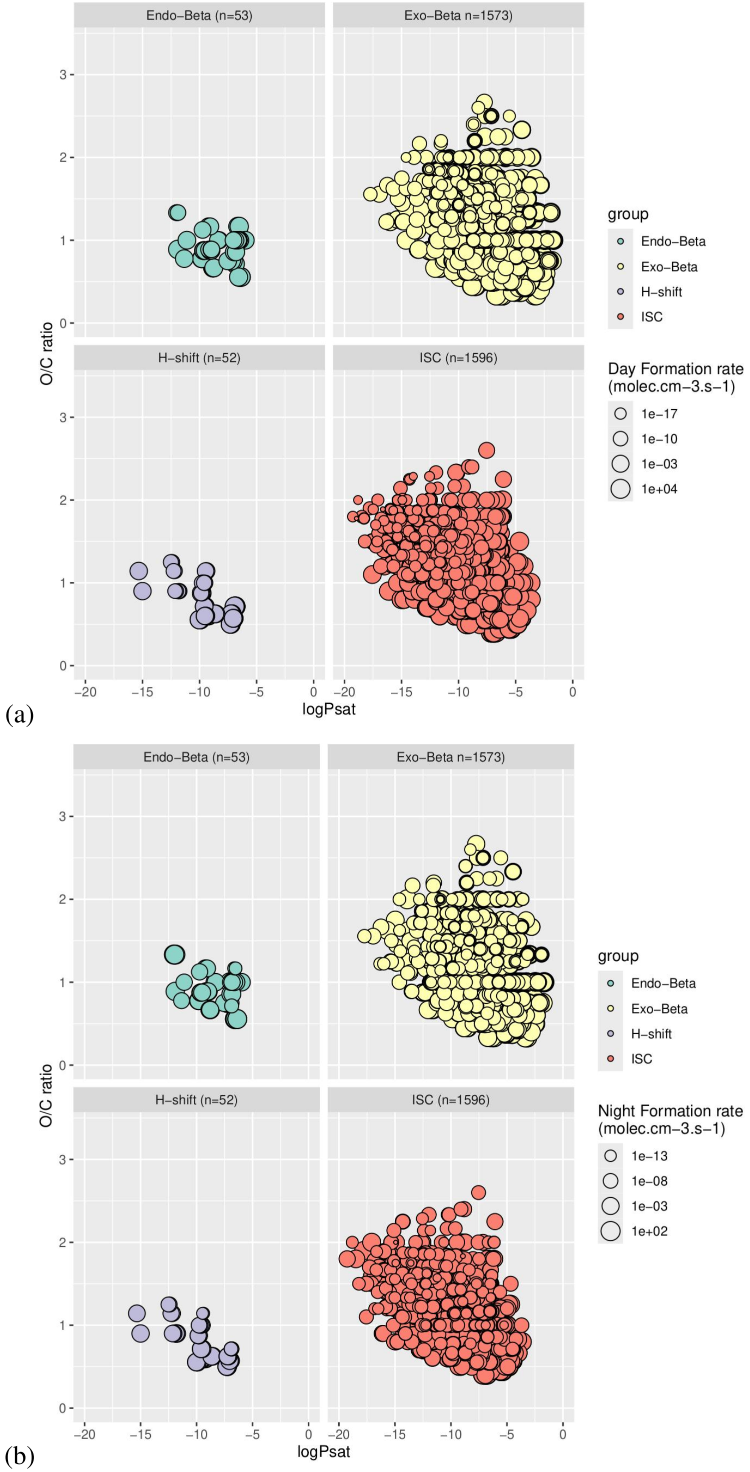

Figure S13. p_{Sat}-distributions of the Isoprene-derived accretion products weighted by the formation rates received from the steady-state calculations.

References

Barley, M. and McFiggans, G.: The critical assessment of vapour pressure estimation methods for use in modelling the formation of atmospheric organic aerosol, Atmospheric Chemistry and Physics, 10, 749–767, 2010.

Bey, I., Aumont, B., and Toupance, G.: The nighttime production of OH radicals in the continental troposphere, Geophysical research letters, 24, 1067–1070, 1997.

Bianchi, F., Kurtén, T., Riva, M., Mohr, C., Rissanen, M. P., Roldin, P., Berndt, T., Crounse, J. D., Wennberg, P. O., Mentel, T. F., et al.: Highly oxygenated organic molecules (HOM) from gas-phase autoxidation involving peroxy radicals: A key contributor to atmospheric aerosol, Chemical reviews, 119, 3472–3509, 2019.

Compernolle, S., Ceulemans, K., and Müller, J.-F.: Vapor pressure estimation methods applied to secondary organic aerosol constituents from α-pinene oxidation: an intercomparison study, Atmospheric Chemistry and Physics, 10, 6271–6282, 2010.

Compernolle, S., Ceulemans, K., and Müller, J.-F.: EVAPORATION: a new vapour pressure estimation methodfor organic molecules including non-additivity and intramolecular interactions, Atmospheric Chemistry and Physics, 11, 9431–9450, 2011.

Eckart, C.: The penetration of a potential barrier by electrons, Physical Review, 35, 1303, 1930.

Franzon, L.: Simple Physical Model for the Estimation of Irreversible Dissociation Rates for Bimolecular Complexes, The Journal of Physical Chemistry A, 127, 5956–5966, 2023.

Grimme, S.: Supramolecular binding thermodynamics by dispersion-corrected density functional theory, Chemistry–A European Journal, 18, 9955–9964, 2012.

Hasan, G.: Computational Studies of Reaction Channels for ^{3}(RO . . . OR) Intermediates formed in Peroxy Self and Cross-Reactions, Ph.D. thesis, University of Helsinki, 2023.

Hasan, G., Salo, V.-T., Golin Almeida, T., Valiev, R. R., and Kurtén, T.: Computational Investigation of Substituent Effects on the Alcohol+ Carbonyl Channel of Peroxy Radical Self-and Cross-Reactions, The Journal of Physical Chemistry A, 127, 1686–1696, 2023.

Ishida, K., Morokuma, K., and Komornicki, A.: The intrinsic reaction coordinate. An ab initio calculation for $HNC \longrightarrow HCN$ and $H-{}^{+}CH_4$, The Journal of Chemical Physics, 66, 2153–2156, 1977.

Jenkin, M. E., Valorso, R., Aumont, B., and Rickard, A. R.: Estimation of rate coefficients and branching ratios for reactions of organic peroxy radicals for use in automated mechanism construction, Atmospheric Chemistry and Physics, 19, 7691–7717, 2019.

Johnston, H. S. and Heicklen, J.: Tunnelling corrections for unsymmetrical Eckart potential energy barriers, The Journal of Physical Chemistry, 66, 532–533, 1962.

Kenagy, H., Heald, C., Tahsini, N., Goss, M., and Kroll, J.: Can we achieve atmospheric chemical environments in the laboratory? An integrated model-measurement approach to chamber SOA studies, In Review, 2024.

Kurtén, T., Tiusanen, K., Roldin, P., Rissanen, M., Luy, J.-N., Boy, M., Ehn, M., and Donahue, N.: α-Pinene autoxidation products may not have extremely low saturation vapor pressures despite high O: C ratios, The Journal of Physical Chemistry A, 120, 2569–2582, 2016.

Lin, Y.-S., Li, G.-D., Mao, S.-P., and Chai, J.-D.: Long-range corrected hybrid density functionals with improved dispersion corrections, Journal of Chemical Theory and Computation, 9, 263–272, 2013.

Møller, K. H., Otkjær, R. V., Hyttinen, N., Kurtén, T., and Kjaergaard, H. G.: Cost-effective implementation of multiconformer transition state theory for peroxy radical hydrogen shift reactions, The Journal of Physical Chemistry A, 120, 10 072–10 087, 2016.

Nannoolal, Y., Rarey, J., Ramjugernath, D., and Cordes, W.: Estimation of pure component properties: Part 1. Estimation of the normal boiling point of non-electrolyte organic compounds via group contributions and group interactions, Fluid Phase Equilibria, 226, 45–63, 2004.

Nannoolal, Y., Rarey, J., and Ramjugernath, D.: Estimation of pure component properties: Part 3. Estimation of the vapor pressure of non-electrolyte organic compounds via group contributions and group interactions, Fluid Phase Equilibria, 269, 117–133, 2008.

Neese, F.: Software update: The ORCA program system - Version 5.0, WIREs Computational Molecular Science, 12, https://doi.org/10.1002/wcms.1606, 2022.

Pankow, J. F. and Asher, W. E.: SIMPOL. 1: a simple group contribution method for predicting vapor pressures and enthalpies of vaporization of multifunctional organic compounds, Atmospheric Chemistry and Physics, 8, 2773–2796, 2008.

Papajak, E., Zheng, J., Xu, X., Leverentz, H. R., and Truhlar, D. G.: Perspectives on basis sets beautiful: Seasonal plantings of diffuse basis functions, Journal of chemical theory and computation, 7, 3027–3034, 2011.

Peräkylä, O., Berndt, T., Franzon, L., Hasan, G., Meder, M., Valiev, R. R., Daub, C. D., Varelas, J. G., Geiger, F. M., Thomson, R. J., et al.: Large Gas-Phase Source of Esters and Other Accretion Products in the Atmosphere, Journal of the American Chemical Society, 145, 7780–7790, 2023.

Pracht, P., Bohle, F., and Grimme, S.: Automated exploration of the low-energy chemical space with fast quantum chemical methods, Physical Chemistry Chemical Physics, 22, 7169–7192, 2020.

Rissanen, M. P., Kurtén, T., Sipilä, M., Thornton, J. A., Kangasluoma, J., Sarnela, N., Junninen, H., Jørgensen, S., Schallhart, S., Kajos, M. K., et al.: The formation of highly oxidized multifunctional products in the ozonolysis of cyclohexene, Journal of the American Chemical Society, 136, 15 596–15 606, 2014.

Seal, P., Barua, S., Iyer, S., Kumar, A., and Rissanen, M.: A systematic study on the kinetics of H-shift reactions in pristine acyl peroxy radicals, Physical Chemistry Chemical Physics, 25, 28 205–28 212, 2023.

Stephens, P. J., Devlin, F. J., Chabalowski, C. F., and Frisch, M. J.: Ab initio calculation of vibrational absorption and circular dichroism spectra using density functional force fields, The Journal of physical chemistry, 98, 11 623–11 627, 1994.

Topping, D.: UManSysProp Multiphase system online property prediction, http://http://umansysprop.seaes.manchester.ac.uk.

Valorso, R., Aumont, B., Camredon, M., Raventos-Duran, T., Mouchel-Vallon, C., Ng, N., Seinfeld, J. H., Lee-Taylor, J., and Madronich, S.: Explicit modelling of SOA formation from α-pinene photooxidation: sensitivity to vapour pressure estimation, Atmospheric Chemistry and Physics, 11, 6895–6910, 2011.

Vereecken, L. and Nozière, B.: H migration in peroxy radicals under atmospheric conditions, Atmospheric chemistry and physics, 20, 7429–7458, 2020.

Vereecken, L. and Peeters, J.: Decomposition of substituted alkoxy radicals—part I: a generalized structure–activity relationship for reaction barrier heights, Physical Chemistry Chemical Physics, 11, 9062–9074, 2009.

Villenave, E., Lesclaux, R., Seefeld, S., and Stockwell, W. R.: Kinetics and atmospheric implications of peroxy radical cross reactions involving the $CH_3C(O)O_2$ radical, Journal of Geophysical Research: Atmospheres, 103, 25 273–25 285, 1998.